

UV-Vis-IR Spectral Complex Refractive Indices and Optical Properties of Brown Carbon Aerosol from Biomass Burning

Benjamin J. Sumlin^{a*}, Yuli W. Heinson^{a*}, Nishit Shetty^a, Apoorva Pandey^a, Robert S. Pattison^b, Stephen Baker^c, Wei Min Hao^c, and Rajan K. Chakrabarty^{a**}

^aCenter for Aerosol Science and Engineering, Department of Energy, Environmental and Chemical Engineering, Washington University in St. Louis, St. Louis, MO 63130

^bUnited States Forest Service, Pacific Northwest Research Station, Anchorage, AK 99501

^cMissoula Fire Sciences Laboratory, United States Forest Service, Missoula, MT 59808

* These authors contributed equally to this work.

** Corresponding author: Rajan K. Chakrabarty (chakrabarty@wustl.edu)

Abstract

Constraining the complex refractive indices, optical properties and size of brown carbon (BrC) aerosols is a vital endeavor for improving climate models and satellite retrieval algorithms. Smoldering wildfires are the largest source of primary BrC, and fuel parameters such as moisture content, source depth, geographic origin, and fuel packing density could influence the properties of the emitted aerosol. We measured *in situ* spectral (375-1047 nm) optical properties of BrC aerosols emitted from smoldering combustion of Boreal and Indonesian peatlands across a range of these fuel parameters. Inverse Lorenz-Mie algorithms used these optical measurements along with simultaneously measured particle size distributions to retrieve the aerosol complex refractive indices ($m=n+i\kappa$). Our results show that the real part n is constrained between 1.5 and 1.7 with no obvious functionality in wavelength (λ), moisture content, source depth, or geographic origin. With increasing λ from 375 to 532 nm, κ decreased from 0.014 to 0.003, with corresponding increase in single scattering albedo (SSA) from 0.93 to 0.99. The spectral variability of κ follows the Kramers-Kronig dispersion relation for a damped harmonic oscillator. For $\lambda \geq 532$ nm, both κ and SSA showed no spectral dependency. We discuss differences between this study and previous work. The imaginary part κ was sensitive to changes in FPD, and we hypothesize mechanisms that might help explain this observation.

Keywords: brown carbon aerosol, complex refractive index, optical properties

1. Introduction

Organic aerosols (OA) account for a large fraction of the total tropospheric particulate matter burden [1, 2]. These aerosols have been typically considered to predominantly scatter light in the visible solar spectrum. However, findings from field [3, 4] and laboratory studies [5, 6] show that a class of OA, optically defined as brown carbon (BrC), significantly absorb in the shorter visible wavelengths ($\lambda \sim 350\text{-}550$ nm) with absorption Ångström exponents (AAE) ranging between 2 and 12 [7]. BrC aerosols have physical, chemical, and optical properties distinct from black carbon (BC) aerosols. BC has a fractal-like morphology with a deep black appearance caused by a significant, non-zero imaginary part κ of its complex refractive index (RI) that is wavelength-independent over the visible and near-visible wavelengths [8]. In contrast, BrC aerosols are spherical in morphology and are yellow-brown in color due to values of κ that increase sharply toward shorter visible and ultraviolet wavelengths. Constraining and parameterizing the spectral optical properties and RIs of BrC aerosols across the solar spectrum has been a challenging endeavor for the atmospheric aerosol community. Climate models and satellite retrieval algorithms rely on this information for accurate retrievals and predictions of aerosol optical depths.

Primary BrC aerosol emissions are largely attributed to biomass and biofuel burning [9-11] and biogenic release of soil and humic matter [7, 12]. In particular, it is the smoldering phase of biomass burning that has been identified as the major source of these particles [10, 13, 14]. Recent studies show that boreal and Indonesian peat fires are the largest contributors of primary BrC aerosols to regional emissions, and contribute up to 72% of all carbon emissions in a given year [15]. Peatlands store between one-fifth and one-third of earth's organic carbon and act as a net carbon sink, but this carbon is increasingly released back to the atmosphere since peatlands face an increasing threat of wildfires due to rising global temperatures [16-18]. Peat fires are dominated by smoldering phase combustion which can persist in low to moderate fuel moisture conditions, and is capable of lasting for several weeks or longer [19].

In this study, we present our results from *in situ*, contact-free measurements of spectral (UV-Vis-IR) optical properties and size distributions of BrC aerosol emitted from laboratory-scale smoldering combustion of peat samples collected from different parts of Alaska and Indonesia. Scattering and absorption coefficients β_{sca} and β_{abs} were measured using four integrated photoacoustic-nephelometers (IPNs). In conjunction with size distribution measurements by a scanning mobility particle sizer (SMPS), these optical measurements were inverted using Mie theory for the retrieval of complex RIs ($m=n+ik$). Best efforts were made to mimic real-world smoldering fire scenarios in our laboratory experiments. Smoldering fire behavior fluctuates across a typical forest floor because of spatial variability in fuel depth, fuel packing density (FPD, mass per unit volume), mineral content, and moisture content (MC) [20-26]. The probability that peat will burn and sustain once ignited depends heavily on MC and FPD. We studied the variation in optical properties and size distributions of emitted smoke aerosols as a function of varying fuel depths, FPDs, and MCs. When compared to previous studies, we find that FPD has the strongest effect on BrC absorption properties, with κ varying directly with FPD. Finally, we constrain

previous literature results and our experimental findings on $\kappa(\lambda)$ using the analytical form of the Kramers-Kronig dispersion relation for a damped harmonic oscillator [27].

2. Experimental methods

Fig. 1 shows the schematic diagram of our experimental setup. The setup consists of a sealed 21 m³ stainless steel chamber equipped with a computer-controlled ignition system and a recirculation fan. The ignition system is a 1 kW ring heater (McMaster-Carr 2927094A) coupled to a 1/16" stainless steel plate, and its temperature is monitored by a K-type thermocouple to close the control loop. We studied peat samples collected from Alaska (AK) and Indonesia (IN). The AK peat samples were separated into collection depths of 0-4" and 4-8" below the surface from sites dominated by sphagnum and black spruce (*Picea mariana*). Typically, canopy cover of black spruce was about 40%. The understory was typically sparse, with species such as dwarf birch (*Betula nana*) and varieties of *Rhododendron* subsect. *Ledum*, *Vaccinium* and *Empetrum*. The AK peat samples were naturally dried to 5%, 10%, 15%, 20%, and 40% MC at room temperature. The IN peat samples were not depth-resolved and were dried to 5%, 20%, and 40% MCs. IN forest speciation information was unavailable due to the high degree of biodiversity in southeast Asian rainforests. Approximately 2 g of each fuel sample was placed on the heating plate such that the FPD was ~ 0.03 g/cm³, and smoldering was initiated by heating the plate to 245 °C. One hour after ignition, aerosols were sampled from ports approximately 2 m above the chamber floor. Gas-phase products were removed with activated parallel-plate semivolatile organic carbon (SVOC) denuders, and excess water was removed with a diffusion dryer packed with indicating silica beads. Finally, the aerosols were mixed in a 208 liter barrel and a homogeneous, isokinetic stream was sampled by each IPN and the SMPS.

The IPNs used in this study are described in detail in the Supporting Material. We operated four custom designed IPNs at $\lambda = 375, 405, 532,$ and 1047 nm. The IPNs measured β_{sca} and β_{abs} continuously with 2 sec time resolution, from which the single scattering albedo (SSA) was calculated. The SMPS measured particle number size distributions every 5-minutes. IPN measurements were averaged over 5 minutes to align with the SMPS measurement intervals.

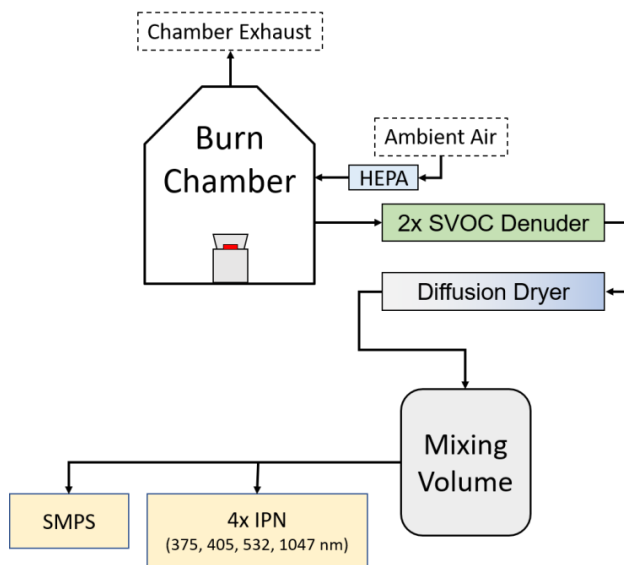


Fig. 1. A schematic diagram of the experimental setup showing the SVOC denuders, diffusion dryer, mixing volume, SMPS, and IPNs.

Complex RI was retrieved using PyMieScatt, a Lorenz-Mie theory package for Python 3 [28]. PyMieScatt includes inversion functions that take measurements of β_{abs} , β_{sca} , and the size distribution to return m . The theory behind the retrieval algorithms is detailed in Ref. 26. To minimize computing overhead, we chose PyMieScatt’s Survey-Iteration algorithm. Briefly, this is a two-stage algorithm that first constructs coarse arrays of $\beta_{abs}(n,\kappa)$ and $\beta_{sca}(n,\kappa)$ for a given size distribution and wavelength of light, and surveys them for values that are close to the IPN measurements. Values with array indices that are common to both the $\beta_{abs}(n,\kappa)$ and $\beta_{sca}(n,\kappa)$ arrays are considered candidate solutions. The iteration stage is best described by Fig. 2. The real part of the refractive index is treated first in the red “Scattering” loop, and then the imaginary part is treated by the blue “Absorption” loop. The algorithm runs for each candidate m found by the survey. When a solution is found, the algorithm reports m along with E_{abs} and E_{sca} , which are the residuals between simulated and measured β_{abs} and β_{sca} .

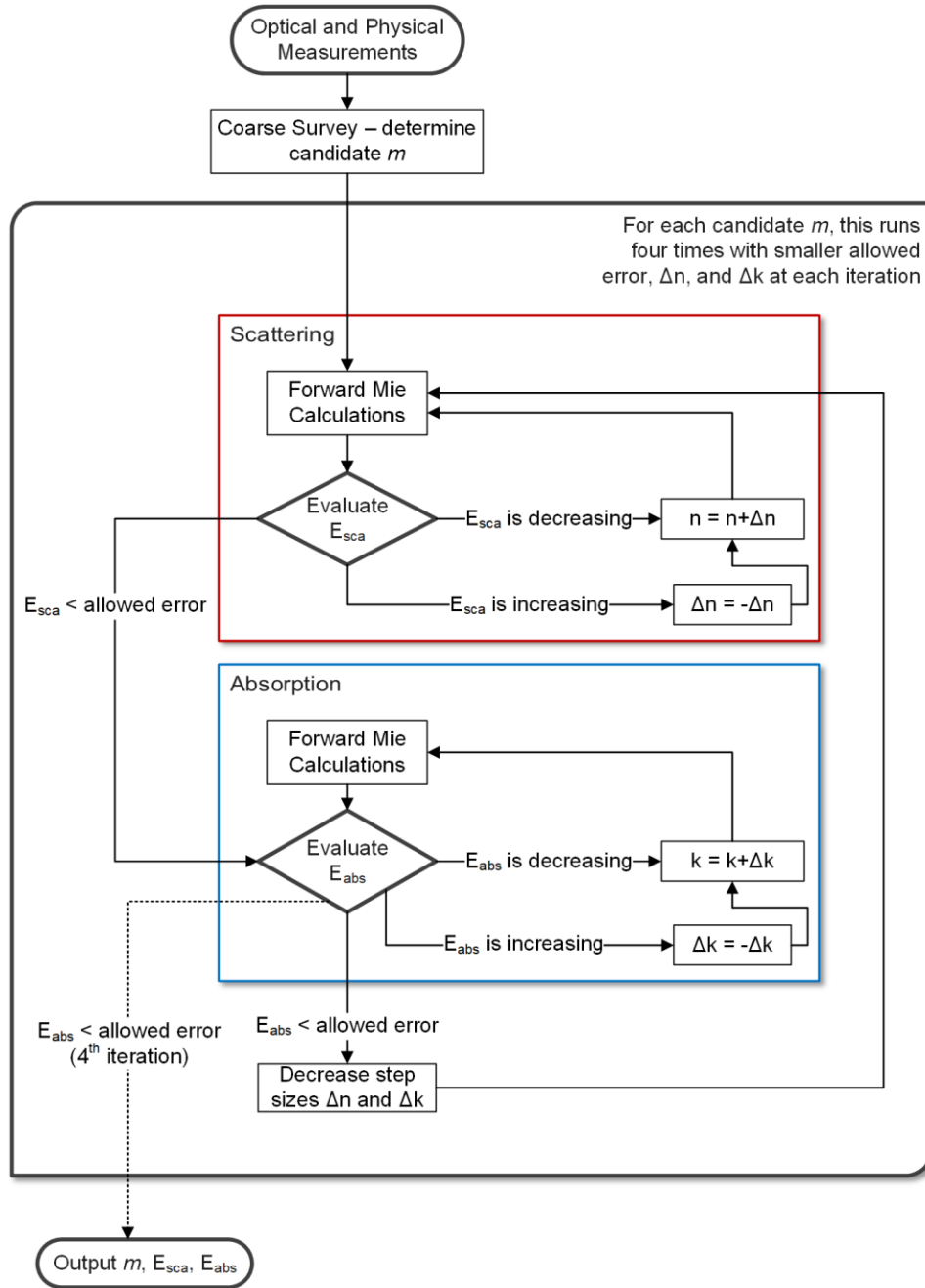


Fig. 2. Flowchart describing the iteration phase of the survey-iteration algorithm. E_{abs} and E_{sca} are the relative errors between measured and simulated β_{abs} and β_{sca} .

We report n and κ as the average of twelve individual retrievals performed in 5-minute data intervals over an hour. Uncertainties for n , κ , SSA, AAE, and κ Ångström exponent (κAE) are propagated through the retrievals and we report the overall standard deviation using

$$\sigma_{\text{overall}} = \sqrt{\frac{\sum_i^N \sigma_i^2}{N}}, \quad (\text{Eq. 1})$$

where σ_i is the standard deviation of each data point and N is the total number of data points.

3. Results and discussion

In this section, we refer to AK peat samples by their MCs and source depths. The IN samples are labelled according to their MCs. The data for all graphs is tabulated in the Supporting Material.

3.1 Complex Refractive Indices

The spectral dependence of m is plotted in Fig. 3. For both AK and IN peat, n is constrained between 1.5 and 1.7, and the spread of data belies any obvious trend in λ . However, we note that n is largely independent of MC, source depth, and geographic origin. We observed no functionality in n or κ as functions of anything other than λ , although in Section 4 we discuss differences in m under varying fuel packing densities.

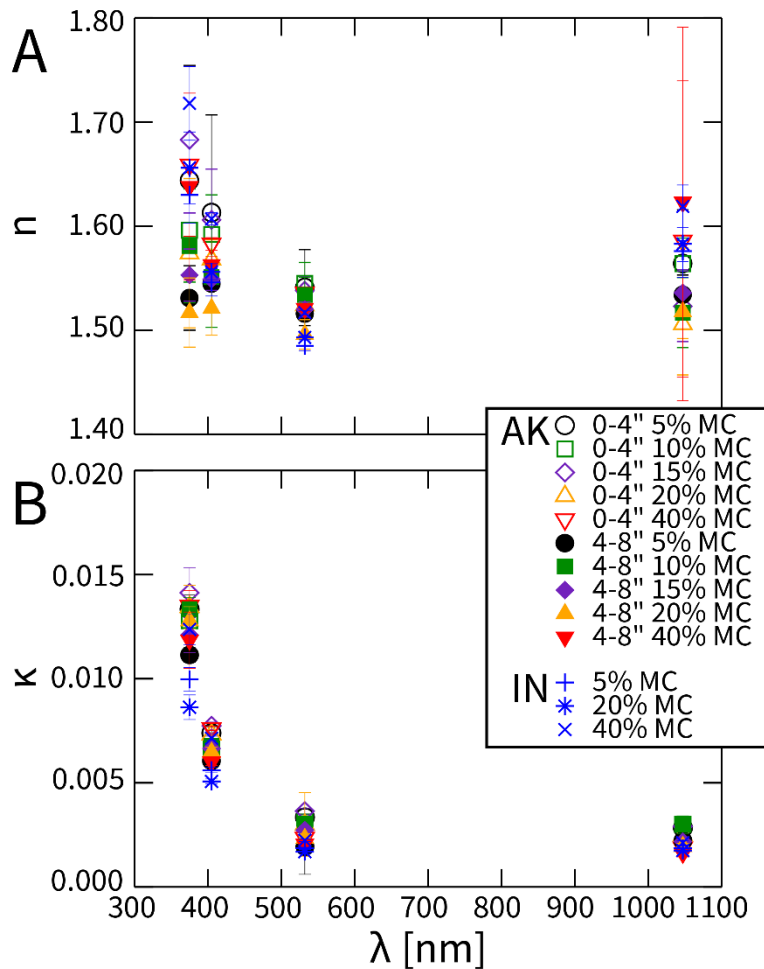


Fig. 3. A: Values of n show no significant dependence on λ , are constrained between 1.5 and 1.7, and are independent of the source depth, MC, and geographic origin. B: κ decreases monotonically with λ between 375 and 532 nm, above which it levels off at $\kappa \approx 0.002$.

The current understanding of BrC optical properties has been summarized in previous work, notably by Liu et al. (2015) and Laskin et al. (2015) [7, 29]. Liu et al. compared the wavelength-dependent κ values for a variety of atmospheric light absorbing organic material such as *m*-xylene and toluene oxidation products [30, 31], as well as BrC from previous studies [32-38]. The κ values we report here, and their sensitivity to change in λ , are commensurate with those previously reported. In fact, when considering κ from this work and averages across the literature referenced by Liu et al., we find that $\kappa(\lambda)$ follows the Kramers-Kronig dispersion relation (KK) for a damped harmonic oscillator [39]. Fig. 4 shows data from this work and the mean of values taken from literature, overlaid with the analytical form of KK given by:

$$\kappa = \frac{a \gamma \nu}{(\nu_0 - \nu)^2 + (\gamma \nu)^2} \quad (\text{Eq. 2})$$

where a is a constant, γ is a line width parameter, ν is the frequency of incident light, and ν_0 is the resonance frequency of the oscillator. Fig. 4 uses $a = 10^{29} \text{ s}^{-2}$ and $\nu_0 = c/\lambda_0$, where $\lambda_0 = 300 \text{ nm}$. The line width parameter γ was set to $2 \times 10^{13} \text{ s}^{-1}$. This function is appropriate near resonance for the BrC absorption spectrum at $375 \leq \lambda \leq 532 \text{ nm}$; far from resonance, i.e. $\lambda = 1047 \text{ nm}$, average κ from literature and this work is 0.002 ± 0.005 .

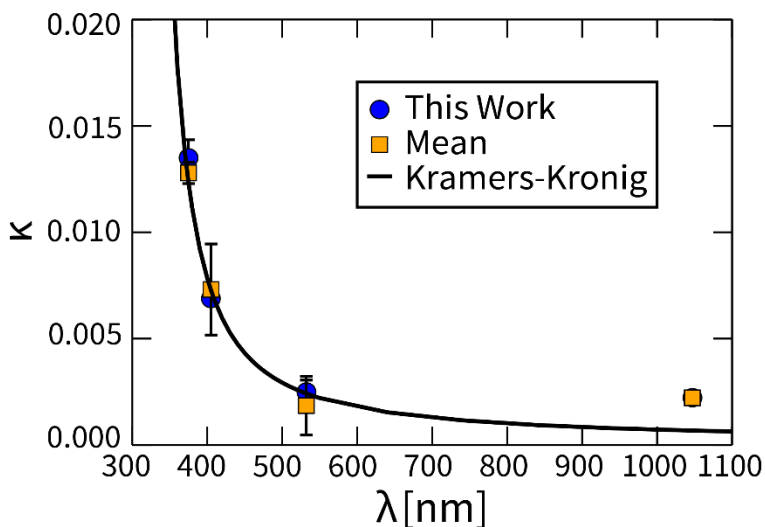


Fig. 4. κ values and the Kramers-Kronig dispersion relation per Eq. 2. The relationship is valid for λ up to 532 nm, beyond which κ appears constant.

3.2 Ångström Exponents

Ångström exponents (AE) can be used to describe the wavelength functionality of any optical parameter that follows a well-behaved power law [39]. For wavelength-independent parameters,

the AE will be between zero and unity, and larger values indicate increasing sensitivity to changes in wavelength [40]. Fig. 5 demonstrates the wavelength dependence of BrC absorption by plotting the κ Ångström exponent (κ AE) and absorption Ångström exponent (AAE) in three intervals of λ (375-405 nm, 405-532 nm, and 532-1047 nm) using the two-wavelength formula:

$$AE(\lambda_1, \lambda_2) = -\frac{\ln \left[\frac{P(\lambda_1)}{P(\lambda_2)} \right]}{\ln \left[\frac{\lambda_1}{\lambda_2} \right]} \quad (\text{Eq. 3})$$

where $P(\lambda)$ is the wavelength-dependent parameter in question, either κ for κ AE or β_{abs} for AAE.

Previous studies have placed BrC κ AE between 4 and 11 [39]. In this study, we find that BrC from peat smoldering is extremely sensitive to wavelength in the near-UV, with a 375-405 nm κ AE values ranging between 7 and 9, while the AAE values range between 8 and 11. Both κ AE and AAE decrease with increasing λ .

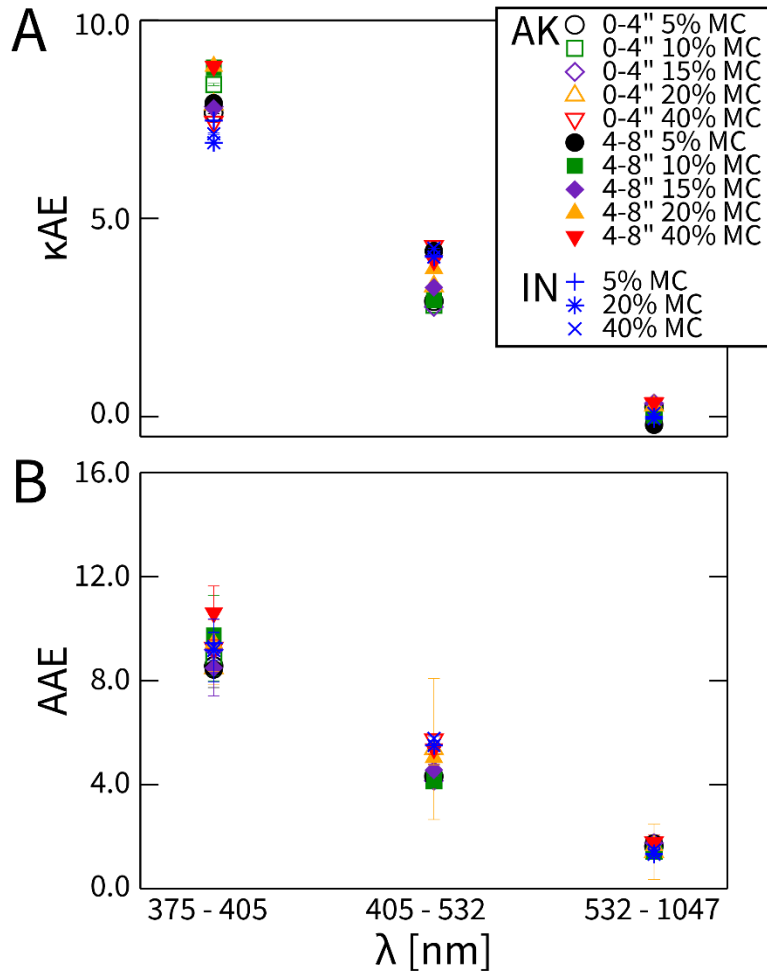


Fig. 5. Ångström exponents as a function of wavelength λ . **A:** κ Ångström exponent (κ AE); **B:** absorption Ångström exponent (AAE).

3.3 Single Scatter Albedo

Given strong κ and weak n functionality with λ , $SSA(\lambda)$ should follow an increasing trend with λ . Indeed, we observe such a trend in Fig. 6. SSA increases with λ until it reaches 0.99 for $\lambda \geq 532$ nm for all peat samples.

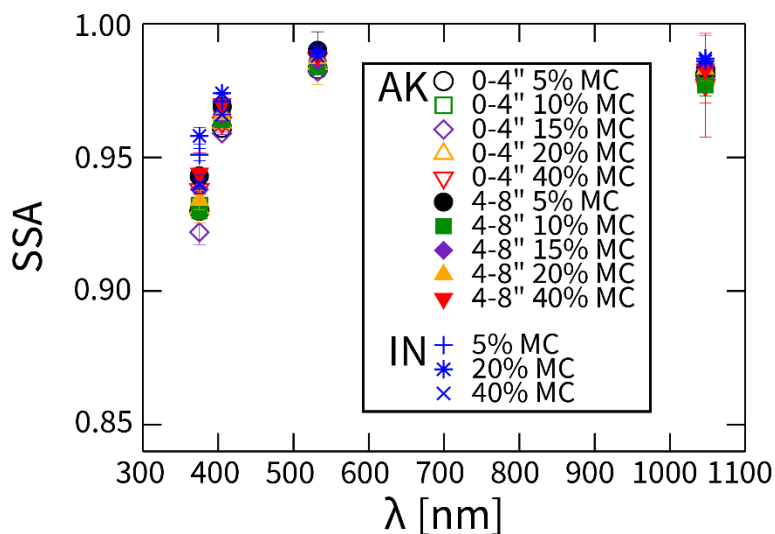


Fig. 6. SSA increases with λ until it reaches a value of 0.99 at $\lambda \geq 532$ nm.

4. Comparisons to previous studies

We compared our findings against previous work that used nearly identical experimental methods to study the effects of atmospheric oxidation on the optical properties of BrC from smoldering combustion [41]. In Ref. [41], the control experiment (fresh, unoxidized BrC) was performed identically to the experiments in this study using AK peat at 5% MC and 0-4" source depth. In the present work, we have shown that BrC optical properties have no functional dependence on MC, source depth, or geographic origin. However, upon comparison to the work in Ref. [41], we find evidence that the fuel packing density (FPD) directly affects m . In this work, fuel was combusted at a packing density of ~ 0.03 g cm⁻³, while in [41], the FPD was ~ 0.06 g cm⁻³, which we term "Low FPD" and "High FPD", respectively. Fig. 7 compares the average n , κ , κAE and AAE of all experiments done in this study to the unaltered BrC emissions from Ref. [41], and in the case of κAE , literature results as well. On average, with higher FPD, n is slightly smaller while κ is significantly larger, which in turn increases both κAE and AAE . We find κ to be 3 times higher at 375 nm, and 1.5 times higher at 405 nm. Fig. 8 shows the comparisons of SSA , a key parameter for climate modelling and satellite retrievals. Densely packed peat, upon smoldering, emits BrC with a lower 375-405 nm SSA , while at $\lambda \geq 532$, both low and high FPD peat BrC have SSA values reaching approximately 0.99.

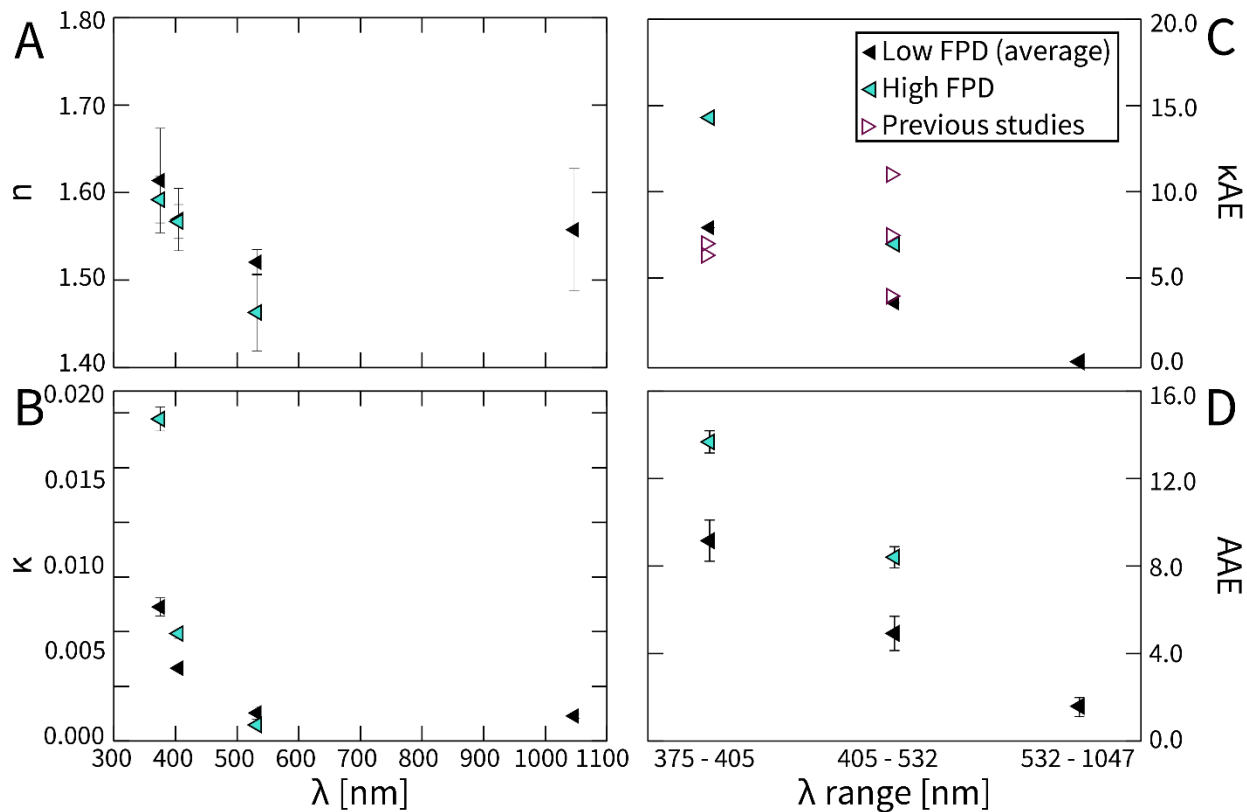


Fig. 7. Comparison of the average results from this study (low FPD, black triangles) to Ref. [41] (high FPD, blue triangles) and other literature results (magenta triangles). **A:** real refractive index n ; **B:** imaginary refractive index κ ; **C:** κ AE; **D:** AAE. BrC from high FPD produced more absorbing and less scattering aerosol, indicated by smaller n and larger κ .

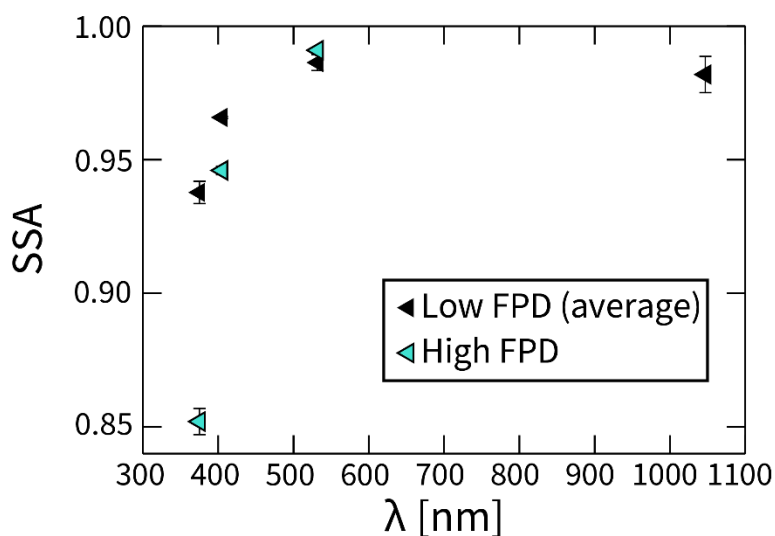


Fig. 8. Comparison of the average SSA from this study (low FPD, black triangles) to Ref. [41] (high FPD, blue triangles). As expected, SSA from both studies increases with wavelength,

although the larger near-UV κ from Ref. [41] results in a lower SSA. At $\lambda \geq 532$, SSA from both studies is nearly 0.99.

Smoldering fire behavior fluctuates across a typical forest floor because of spatial variability in fuel depth, fuel packing density (FPD), mineral content, and MC [20, 22, 23, 42-44]. Combustion in a thick bed of peat is typically stratified, and flame front velocities depend on the depth at which the fire occurs [45]. We hypothesize that denser fuel packing would slow the velocity of the flame front through the fuel layers. The preheat zone ahead of the flame front would then expand as heat is transported away into uncombusted fuel. This larger preheat zone may volatilize organic compounds ahead of combustion, creating a VOC-rich zone entrained within the fuel through which particles created by combustion must travel, with the least volatile compounds emitted just ahead of combustion. These VOCs may condense on the particle, altering their mean molecular weight and speciation, and consequently modify their absorption behavior. However, FPD may simply be a proxy for oxygen availability. When the FPD was $\sim 0.06 \text{ g/cm}^3$ —corresponding to a 3/4" thick fuel packing on the heating plate—the smoldering front propagated slowly due to limited oxygen, which, by the mechanisms hypothesized, may produce higher molecular weight compounds with larger κ values. Conversely, when the FPD was $\sim 0.03 \text{ g/cm}^3$, the environment was comparatively oxygen-rich, resulting in more rapid combustion and production of lower molecular weight compounds with smaller κ values. These hypotheses will be a subject of future research.

5. Concluding remarks and future work

We conducted *in situ* contact-free measurements of spectral optical properties of primary BrC aerosols emitted from smoldering combustion of peat samples collected from different parts of Alaska and Indonesia. Using optical and physical measurements, we retrieved the complex RIs of those aerosols using an inverse Mie algorithm and sought dependencies on MC, source depth, and geography. We found that BrC optical properties are not sensitive to these parameters, suggesting that climate models and satellite retrievals can make use of a smaller parameter space when considering BrC aerosol emitted from biomass burning. However, we found a novel relationship between the complex RIs and the FPD, with more densely packed fuel producing more highly-absorbing aerosols.

We expect FPD will vary widely in a real-world peat bog. The degree of fuel packing may vary across many orders of magnitude in a small area, and therefore future work is needed to draw quantitative conclusions between FPD and its effect on the optical properties of the emitted BrC, as well as to understand what this may mean for the broader impacts of BrC from smoldering wildfires.

Acknowledgements

This work was partially supported by the National Science Foundation under Grant No. AGS1455215, NASA ROSES under Grant No. NNX15AI66G, and the International Center for Energy, Environment and Sustainability (InCEES) at Washington University in St. Louis.

Data Availability

Tabulated data is available in the SM. The computer code used for refractive index retrievals is described in [28] and is available at <https://github.com/bsumlin/PyMieScatt>. Raw data is available from the authors upon request.

References

- [1] Kanakidou M, Seinfeld JH, Pandis SN, Barnes I, Dentener FJ, Facchini MC, et al. Organic aerosol and global climate modelling: a review. *Atmos Chem Phys*. 2005;5:1053-123.
- [2] Jimenez JL, Canagaratna MR, Donahue NM, Prevot ASH, Zhang Q, Kroll JH, et al. Evolution of Organic Aerosols in the Atmosphere. *Science*. 2009;326:1525-9.
- [3] Eck TF, Holben BN, Reid JS, Sinyuk A, Hyer EJ, O'Neill NT, et al. Optical properties of boreal region biomass burning aerosols in central Alaska and seasonal variation of aerosol optical depth at an Arctic coastal site. *Journal of Geophysical Research: Atmospheres*. 2009;114.
- [4] Pfister GG, Hess PG, Emmons LK, Rasch PJ, Vitt FM. Impact of the summer 2004 Alaska fires on top of the atmosphere clear-sky radiation fluxes. *Journal of Geophysical Research: Atmospheres*. 2008;113.
- [5] Chakrabarty RK, Gyawali M, Yatavelli RLN, Pandey A, Watts AC, Knue J, et al. Brown carbon aerosols from burning of boreal peatlands: microphysical properties, emission factors, and implications for direct radiative forcing. *Atmos Chem Phys*. 2016;16:3033-40.
- [6] Chand D, Schmid O, Gwaze P, Parmar RS, Helas G, Zeromskiene K, et al. Laboratory measurements of smoke optical properties from the burning of Indonesian peat and other types of biomass. *Geophysical Research Letters*. 2005;32.
- [7] Laskin A, Laskin J, Nizkorodov SA. Chemistry of Atmospheric Brown Carbon. *Chem Rev*. 2015;115:4335-82.
- [8] Moosmuller H, Chakrabarty RK, Arnott WP. Aerosol light absorption and its measurement: A review. *J Quant Spectrosc Ra*. 2009;110:844-78.
- [9] Ramanathan V, Li F, Ramana MV, Praveen PS, Kim D, Corrigan CE, et al. Atmospheric brown clouds: Hemispherical and regional variations in long-range transport, absorption, and radiative forcing. *Journal of Geophysical Research: Atmospheres*. 2007;112.
- [10] Chakrabarty RK, Moosmueller H, Chen LWA, Lewis K, Arnott WP, Mazzoleni C, et al. Brown carbon in tar balls from smoldering biomass combustion. *Atmospheric Chemistry and Physics*. 2010;10:6363-70.
- [11] Lack DA, Langridge JM, Bahreini R, Cappa CD, Middlebrook AM, Schwarz JP. Brown carbon and internal mixing in biomass burning particles. *Proc Natl Acad Sci U S A*. 2012;109:14802-7.

- [12] Veghte DP, China S, Weis J, Kovarik L, Gilles MK, Laskin A. Optical Properties of Airborne Soil Organic Particles. ACS Earth and Space Chemistry. 2017.
- [13] Einfeld W, Ward, D.E., & Hardy, C. Levine, J.S. Effects of fire behavior on prescribed fire smoke characteristics: A case study: Massachusetts Inst of Tech Press; 1991.
- [14] Bond TC, Streets DG, Yarber KR, Nelson SM, Woo J-H, Klimont Z. A technology-based global inventory of black and organic carbon emissions from combustion. J Geophys Res (USA). 2004;109:43-pp.
- [15] Kasischke ES, Hyer EJ, Novelli PC, Bruhwiler LP, French NHF, Sukhinin AI, et al. Influences of boreal fire emissions on Northern Hemisphere atmospheric carbon and carbon monoxide. Glob Biogeochem Cycle. 2005;19.
- [16] Turetsky MR, Benscoter B, Page S, Rein G, van der Werf GR, Watts A. Global vulnerability of peatlands to fire and carbon loss. Nature Geosci. 2015;8:11-4.
- [17] Kharuk VI, Ranson KJ, Dvinskaya ML. Wildfires dynamic in the larch dominance zone. Geophysical Research Letters. 2008;35.
- [18] Climate change 2007: the physical science basis: contribution of Working Group I to the Fourth Assessment Report of the Intergovernmental Panel on Climate Change 2007: Cambridge Univ Press.
- [19] Bertschi I, Yokelson RJ, Ward DE, Babbitt RE, Susott RA, Goode JG, et al. Trace gas and particle emissions from fires in large diameter and belowground biomass fuels. Journal of Geophysical Research: Atmospheres. 2003;108.
- [20] Wagner CEV. Duff Consumption by Fire in Eastern Pine Stands. Canadian Journal of Forest Research. 1972;2:34-9.
- [21] Shafizadeh F, DeGroot WF. COMBUSTION CHARACTERISTICS OF CELLULOSIC FUELS. Thermal Uses and Properties of Carbohydrates and Lignins: Academic Press; 1976. p. 1-17.
- [22] Wein RW. Characteristics and suppression of fires in organic terrain in Australia. Australian Forestry. 1981;44:162-9.
- [23] Frandsen WH, Ryan KC. Soil moisture reduces belowground heat flux and soil temperatures under a burning fuel pile. Canadian Journal of Forest Research. 1986;16:244-8.
- [24] Latham DJ, Schlieter JA, Station IR. Ignition Probabilities of Wildland Fuels Based on Simulated Lightning Discharges: U.S. Department of Agriculture, Forest Service, Intermountain Research Station; 1989.
- [25] Hartford RA, Frandsen WH. When It's Hot, It's Hot... Or Maybe It's Not! (Surface Flaming May Not Portend Extensive Soil Heating)1992.

- [26] Hartford RA. "Smoldering combustion limits in peat as influenced by moisture mineral content and organic bulk density: The University of Montana; 1993.
- [27] Demtröder W. Laser Spectroscopy: Basic Concepts and Instrumentation. 3 ed. Berlin, Heidelberg, New York: Springer Verlag; 2003.
- [28] Sumlin BJ, Heinson WR, Chakrabarty RK. Retrieving the aerosol complex refractive index using PyMieScatt: A Mie computational package with visualization capabilities. *Journal of Quantitative Spectroscopy and Radiative Transfer*. 2018;205:127-34.
- [29] Liu PF, Abdelmalki N, Hung HM, Wang Y, Brune WH, Martin ST. Ultraviolet and visible complex refractive indices of secondary organic material produced by photooxidation of the aromatic compounds toluene and *m*-xylene. *Atmospheric Chemistry and Physics*. 2015;15:1435-46.
- [30] Liu P, Zhang Y, Martin ST. Complex Refractive Indices of Thin Films of Secondary Organic Materials by Spectroscopic Ellipsometry from 220 to 1200 nm. *Environmental Science & Technology*. 2013;47:13594-601.
- [31] Liu J, Bergin M, Guo H, King L, Kotra N, Edgerton E, et al. Size-resolved measurements of brown carbon in water and methanol extracts and estimates of their contribution to ambient fine-particle light absorption. *Atmospheric Chemistry and Physics*. 2013;13:12389-404.
- [32] Alexander DTL, Crozier PA, Anderson JR. Brown Carbon Spheres in East Asian Outflow and Their Optical Properties. *Science*. 2008;321:833-6.
- [33] Kirchstetter TW, Novakov T, Hobbs PV. Evidence that the spectral dependence of light absorption by aerosols is affected by organic carbon. *Journal of Geophysical Research: Atmospheres*. 2004;109.
- [34] Chakrabarty R, Moosmüller H, Chen L-W, Lewis K, Arnott W, Mazzoleni C, et al. Brown carbon in tar balls from smoldering biomass combustion. *Atmospheric Chemistry and Physics*. 2010;10:6363-70.
- [35] Lack DA, Bahreni R, Langridge JM, Gilman JB, Middlebrook AM. Brown carbon absorption linked to organic mass tracers in biomass burning particles. *Atmospheric Chemistry and Physics*. 2013;13:2415-22.
- [36] Hoffer A, Gelencsér A, Guyon P, Kiss G, Schmid O, Frank GP, et al. Optical properties of humic-like substances (HULIS) in biomass-burning aerosols. *Atmospheric Chemistry and Physics*. 2006;6:3563-70.
- [37] Dinar E, Abo Riziq A, Spindler C, Erlick C, Kiss G, Rudich Y. The complex refractive index of atmospheric and model humic-like substances (HULIS) retrieved by a cavity ring down aerosol spectrometer (CRD-AS). *Faraday Discuss*. 2008;137:279-95.

- [38] Cappa CD, Onasch TB, Massoli P, Worsnop DR, Bates TS, Cross ES, et al. Radiative absorption enhancements due to the mixing state of atmospheric black carbon. *Science*. 2012;337:1078-81.
- [39] Moosmüller H, Chakrabarty RK, Ehlers KM, Arnott WP. Absorption Ångström coefficient, brown carbon, and aerosols: basic concepts, bulk matter, and spherical particles. *Atmos Chem Phys*. 2011;11:1217-25.
- [40] Kerker M. *The Scattering of Light and Other Electromagnetic Radiation*: Academic Press; 1969.
- [41] Sumlin BJ, Pandey A, Walker MJ, Pattison RS, Williams BJ, Chakrabarty RK. Atmospheric Photooxidation Diminishes Light Absorption by Primary Brown Carbon Aerosol from Biomass Burning. *Environ Sci Tech Let*. 2017;4:540-5.
- [42] Shafizadeh F, DeGroot WF. *Combustion Characteristics of Cellulosic Fuels. Thermal Uses and Properties of Carbohydrates and Lignins*: Elsevier; 1976. p. 1-17.
- [43] Hartford RA, Frandsen WH. When It's Hot, It's Hot... Or Maybe It's Not! (Surface Flaming May Not Portend Extensive Soil Heating). *International Journal of Wildland Fire*. 1992;2:139.
- [44] Hartford RA. *Smoldering combustion limits in peat as influenced by moisture mineral content and organic bulk density*. The University of Montana: The University of Montana; 1993.
- [45] Usup A, Hashimoto Y, Takahashi H, Hayasaka H. Combustion and thermal characteristics of peat fire in tropical peatland in Central Kalimantan, Indonesia. *Tropics*. 2004;14:1-19.

Supporting Material for

UV-Vis-IR Spectral Complex Refractive Indices and Optical Properties of Brown Carbon Aerosol from Biomass Burning

Benjamin J. Sumlin^{a*}, Yuli W. Heinson^{a*}, Nishit Shetty^a, Apoorva Pandey^a, Robert S. Pattison^b, Stephen Baker^c, Wei Min Hao^c, and Rajan K. Chakrabarty^{a**}

^aDepartment of Energy, Environmental and Chemical Engineering, Washington University in St. Louis, St. Louis, MO 63130

^bUnited States Forest Service, Pacific Northwest Research Station, Anchorage, AK 99501

^cMissoula Fire Sciences Laboratory, United States Forest Service, Missoula, MT 59808

* These authors contributed equally to this work.

** Corresponding author: Rajan K. Chakrabarty (chakrabarty@wustl.edu)

1. Instrumentation

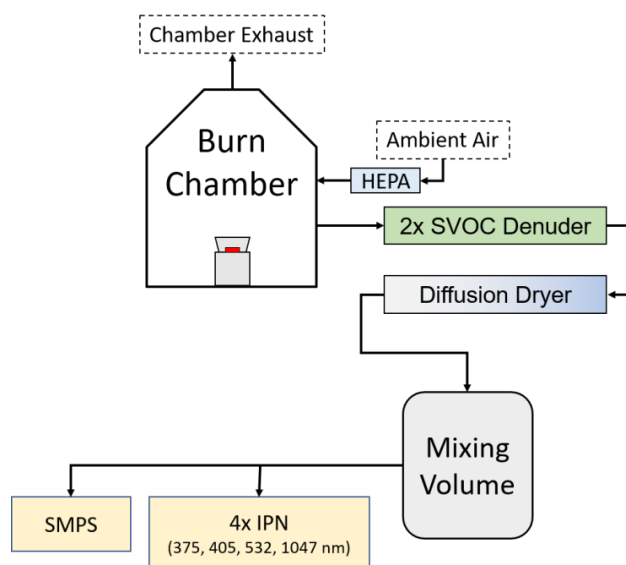


Fig. S1. The experimental setup.

Fig. S1 shows the schematic diagram of our experimental setup. The setup consists of a sealed 21 m³ stainless steel chamber equipped with a computer-controlled ignition system and a recirculation fan. The ignition system is a 1 kW ring heater (McMaster-Carr 2927094A) coupled to a 1/16" stainless steel plate, and its temperature is monitored by a K-type thermocouple to close the control loop. One hour after ignition, aerosols were sampled from ports approximately 2 m above the chamber floor. Gas-phase products were removed with activated carbon parallel-plate denuders (Sunset Laboratory Inc., Tigard, OR), and excess water was removed with a diffusion dryer packed with indicating silica beads (McMaster-Carr part 2181K97). Finally, the aerosols were mixed in a 208 liter barrel (McMaster-Carr part 4392T47). Sampling took place directly from the mixing volume from ports connected to the circumference of the barrel at half the barrel height. Instrumentation was comprised of four integrated photoacoustic spectrometer/nephelometers (IPN) at 375, 405, 532, and 1047 nm, a scanning mobility particle sizer (SMPS, TSI, Inc., Shoreview, MN). The residence time distribution for the experimental setup was measured, and from this information we determined that one hour after ignition was the optimal time frame to begin data collection.

1.1 Integrated photoacoustic-nephelometer (IPN)

Photoacoustic spectroscopy and nephelometry have been widely applied to measure absorption and scattering of light by aerosols, and working principles and calibration methods are well documented in the literature [1-14]. The integrated photoacoustic-nephelometer (IPN) spectrometer is an in-situ, real-time, contact-free measurement that gives highly precise values of light scattering and absorption coefficients β_{sca} and β_{abs} at a single wavelength. In this study, single-pass IPN spectrometers of our own design were used.

The IPN measures β_{abs} by the photoacoustic effect and β_{sca} via an integrating nephelometer. The photoacoustic portion was designed and calibrated based on Arnott et al. (1999), with additional considerations for design and optimization from Arnott et al. (2006) [2, 4]. It utilizes a $\frac{1}{2}$ -wavelength plane-wave longitudinal resonator with the microphone and calibration speaker placed at pressure antinodes.

The integrated nephelometer was designed and calibrated based on Penaloza (1999) and Abu-Rahmah et al. (2006), and has a truncation angle of approximately 5° [9, 14]. The sensor is a silicon photodiode with a Teflon cosine lens.

Data were acquired at 2 s intervals and instrument zeros were obtained every 300 measurements. The zeroing process involves automatically switching from sample flow to HEPA-filtered flow via a mechanically-controlled valve actuated by the instrument software. The background measurement is averaged over 30 s to improve the signal-to-noise ratio for zeroing. Since the zeroing filter does not effectively remove gaseous species, excess ozone and NO_x compounds are included in the instrument backgrounds and their interferences with absorption measurements are neglected during regular sampling.

The resonant frequency f_0 and quality factor Q are explicit functions of ambient conditions (namely temperature, pressure, and relative humidity) which are subject to fluctuations, even in a climate-controlled laboratory study. The IPN zeroing process measures f_0 and Q during zeroing by playing a chirp into the cell and determining the frequency where sound pressure is a maximum.

Calibrations are performed as commonly done in the literature, with non-absorbing aerosols (salt) to calibrate scattering, and absorbing aerosols (kerosene soot) to calibrate absorption. The slope of a linear regression of scattering versus extinction is the calibration factor for scattering, while the slope of absorption versus extinction-minus-scattering is used for absorption.

Raw data was post-processed to 5-minute averages, commensurate with the scan times of the SMPS. These 5-minute averages were used to determine the complex refractive indices ($m=n+i\kappa$) and single-scatter albedo (SSA).

2. Tabulated Data

Table S1. Complex refractive indices ($m=n+ik$) and single scatter albedo (SSA) for AK peat. Values are averages \pm one standard deviation.

λ (nm)	Depth (inches)	MC (%)	n	k	SSA
375	0 - 4	5	1.644 ± 0.110	0.01334 ± 0.00068	0.930 ± 0.002
		10	1.596 ± 0.050	0.01279 ± 0.00092	0.932 ± 0.005
		15	1.683 ± 0.070	0.01413 ± 0.00120	0.922 ± 0.005
		20	1.574 ± 0.072	0.01344 ± 0.00104	0.931 ± 0.006
		40	1.659 ± 0.069	0.01351 ± 0.00073	0.938 ± 0.004
	4 - 8	5	1.531 ± 0.031	0.01114 ± 0.00035	0.943 ± 0.002
		10	1.581 ± 0.055	0.01334 ± 0.00055	0.930 ± 0.003
		15	1.553 ± 0.025	0.01210 ± 0.00085	0.938 ± 0.004
		20	1.517 ± 0.033	0.01278 ± 0.00068	0.934 ± 0.004
		40	1.638 ± 0.090	0.01185 ± 0.00135	0.944 ± 0.008
405	0 - 4	5	1.613 ± 0.094	0.00739 ± 0.00031	0.961 ± 0.001
		10	1.592 ± 0.038	0.00671 ± 0.00016	0.964 ± 0.001
		15	1.606 ± 0.049	0.00774 ± 0.00018	0.982 ± 0.001
		20	1.568 ± 0.019	0.00733 ± 0.00001	0.963 ± 0.001
		40	1.583 ± 0.006	0.00762 ± 0.00010	0.963 ± 0.001
	4 - 8	5	1.545 ± 0.004	0.00606 ± 0.00012	0.969 ± 0.001
		10	1.551 ± 0.048	0.00677 ± 0.00020	0.964 ± 0.001
		15	1.549 ± 0.011	0.00665 ± 0.00001	0.966 ± 0.001
		20	1.521 ± 0.026	0.00647 ± 0.00024	0.966 ± 0.001
		40	1.563 ± 0.008	0.00600 ± 0.00016	0.970 ± 0.001
532	0 - 4	5	1.541 ± 0.036	0.00334 ± 0.00012	0.983 ± 0.001
		10	1.545 ± 0.020	0.00312 ± 0.00023	0.984 ± 0.001
		15	1.538 ± 0.013	0.00364 ± 0.00015	0.982 ± 0.001
		20	1.524 ± 0.014	0.00299 ± 0.00153	0.985 ± 0.008
		40	1.536 ± 0.004	0.00236 ± 0.00011	0.987 ± 0.001
	4 - 8	5	1.516 ± 0.003	0.00194 ± 0.00133	0.990 ± 0.007
		10	1.534 ± 0.017	0.00304 ± 0.00022	0.984 ± 0.001
		15	1.520 ± 0.007	0.00273 ± 0.00018	0.986 ± 0.001
		20	1.496 ± 0.014	0.00233 ± 0.00023	0.987 ± 0.001
		40	1.521 ± 0.003	0.00205 ± 0.00010	0.988 ± 0.001
1047	0 - 4	5	1.564 ± 0.052	0.00284 ± 0.00027	0.981 ± 0.002
		10	1.564 ± 0.025	0.00301 ± 0.00023	0.980 ± 0.001
		15	1.523 ± 0.034	0.00290 ± 0.00019	0.979 ± 0.002
		20	1.506 ± 0.014	0.00247 ± 0.00022	0.980 ± 0.002
		40	1.586 ± 0.154	0.00188 ± 0.00023	0.977 ± 0.019
	4 - 8	5	1.534 ± 0.019	0.00222 ± 0.00024	0.983 ± 0.002
		10	1.517 ± 0.034	0.00299 ± 0.00042	0.977 ± 0.004
		15	1.536 ± 0.022	0.00218 ± 0.00023	0.986 ± 0.001
		20	1.518 ± 0.061	0.00194 ± 0.00015	0.983 ± 0.005

		40	1.623 ± 0.168	0.00161 ± 0.00017	0.983 ± 0.013
--	--	----	-------------------	-----------------------	-------------------

Table S2. m and SSA for IN peat. Values are averages \pm one standard deviation.

λ (nm)	MC (%)	n	κ	SSA
375	5	1.630 ± 0.027	0.00997 ± 0.00058	0.951 ± 0.002
	20	1.656 ± 0.034	0.00863 ± 0.00059	0.958 ± 0.003
	40	1.718 ± 0.035	0.01237 ± 0.00075	0.940 ± 0.001
405	5	1.546 ± 0.013	0.00561 ± 0.00013	0.971 ± 0.001
	20	1.556 ± 0.008	0.00507 ± 0.00012	0.974 ± 0.001
	40	1.607 ± 0.006	0.00714 ± 0.00010	0.966 ± 0.001
532	5	1.485 ± 0.005	0.00186 ± 0.00001	0.989 ± 0.001
	20	1.493 ± 0.002	0.00169 ± 0.00001	0.990 ± 0.001
	40	1.517 ± 0.002	0.00224 ± 0.00001	0.988 ± 0.001
1047	5	1.576 ± 0.010	0.00186 ± 0.00001	0.986 ± 0.001
	20	1.583 ± 0.032	0.00175 ± 0.00001	0.987 ± 0.001
	40	1.619 ± 0.0205	0.00212 ± 0.00011	0.986 ± 0.001

Table S3. Absorption Ångström Exponents (AAE) for AK peat. Values are averages \pm one standard deviation.

λ range (nm)	Depth (inches)	MC (%)	AAE
375 - 405	0 - 4	5	8.566 ± 0.404
		10	8.941 ± 0.949
		15	9.188 ± 0.808
		20	8.483 ± 0.621
		40	9.256 ± 1.093
	4 - 8	5	8.425 ± 0.689
		10	9.740 ± 1.541
		15	8.494 ± 1.079
		20	9.448 ± 1.086
		40	10.600 ± 1.040
405 - 532	0 - 4	5	4.326 ± 0.172
		10	4.155 ± 0.290
		15	4.154 ± 0.188
		20	5.371 ± 2.710
		40	5.737 ± 0.226
	4 - 8	5	4.275 ± 0.263
		10	4.181 ± 0.314
		15	4.566 ± 0.229
		20	5.043 ± 0.290
		40	5.382 ± 0.209
532 - 1047	0 - 4	5	1.641 ± 0.125
		10	1.450 ± 0.197
		15	1.755 ± 0.127

		20	1.421 ± 1.067
		40	1.796 ± 0.266
	4 - 8	5	1.740 ± 0.164
		10	1.467 ± 0.267
		15	1.758 ± 0.210
		20	1.659 ± 0.204
		40	1.773 ± 0.131

Table S4. AAE for IN peat. Values are averages \pm one standard deviation.

λ range (nm)	MC (%)	AAE
375 - 405	5	9.439 ± 0.436
	20	9.165 ± 1.208
	40	9.305 ± 0.519
405 - 532	5	5.503 ± 0.087
	20	5.510 ± 0.148
	40	5.781 ± 0.075
532 - 1047	5	1.355 ± 0.122
	20	1.331 ± 0.171
	40	1.473 ± 0.128

Table S5. κ Ångström Exponents (κ AE) for AK peat. Values are averages \pm one standard deviation.

λ range (nm)	Depth (inches)	MC (%)	κ AE
375 - 405	0 - 4	5	7.675 ± 0.002
		10	8.382 ± 0.002
		15	7.821 ± 0.003
		20	7.877 ± 0.002
		40	7.441 ± 0.001
	4 - 8	5	7.911 ± 0.001
		10	8.813 ± 0.001
		15	7.778 ± 0.002
		20	8.845 ± 0.002
		40	8.843 ± 0.003
405 - 532	0 - 4	5	2.912 ± 0.001
		10	2.808 ± 0.001
		15	2.766 ± 0.001
		20	3.228 ± 0.004
		40	4.297 ± 0.001
	4 - 8	5	4.176 ± 0.005
		10	2.935 ± 0.001
		15	3.264 ± 0.001
		20	3.744 ± 0.001
		40	3.937 ± 0.001
532 - 1047	0 - 4	5	0.240 ± 0.000
		10	0.053 ± 0.000

		15	0.336 ± 0.000
		20	0.282 ± 0.002
		40	0.336 ± 0.000
	4 - 8	5	-0.199 ± 0.001
		10	0.024 ± 0.001
		15	0.332 ± 0.001
		20	0.271 ± 0.000
		40	0.357 ± 0.000

Table S6. κ AE for IN peat. Values are averages \pm one standard deviation.

λ range (nm)	MC (%)	κ AE
375 - 405	5	7.472 ± 0.001
	20	6.911 ± 0.001
	40	7.141 ± 0.001
405 - 532	5	4.047 ± 0.001
	20	4.028 ± 0.001
	40	4.250 ± 0.001
532 - 1047	5	0.000 ± 0.000
	20	-0.052 ± 0.000
	40	0.081 ± 0.000

Table S7. Complex refractive index ($m=n+i\kappa$) and single scattering albedo (SSA) for high FPD AK peat (fuel packing density $\sim 0.06 \text{ g cm}^{-3}$) from Sumlin et al. (2017) [15]. Values are averages \pm one standard deviation.

λ (nm)	n	κ	SSA
375	1.592 ± 0.027	0.02945 ± 0.00110	0.852 ± 0.005
405	1.567 ± 0.019	0.00983 ± 0.00044	0.946 ± 0.002
532	1.463 ± 0.044	0.00147 ± 0.00016	0.991 ± 0.001

Table S8. Absorption Ångström Exponents (AAE) for high FPD AK peat from Sumlin et al. (2017). Values are averages \pm one standard deviation.

λ range (nm)	AAE
375 - 405	13.678 ± 0.505
405 - 532	8.406 ± 0.484

Table S9. κ Ångström Exponents (κ AE) for high FPD AK peat from Sumlin et al. (2017). Values are averages \pm one standard deviation.

λ range (nm)	κ AE
375 - 405	14.257 ± 0.005
405 - 532	6.967 ± 0.004

References

- [1] Arnott WP, Hamasha K, Moosmüller H, Sheridan PJ, Ogren JA. Towards aerosol light-absorption measurements with a 7-wavelength aethalometer: Evaluation with a photoacoustic instrument and 3-wavelength nephelometer. *Aerosol Science and Technology*. 2005;39:17-29.
- [2] Arnott WP, Moosmüller H, Fred Rogers C, Jin T, Bruch R. Photoacoustic spectrometer for measuring light absorption by aerosol: instrument description. *Atmos Environ*. 1999;33:2845-52.
- [3] Arnott WP, Moosmüller H, Walker JW. Nitrogen dioxide and kerosene-flame soot calibration of photoacoustic instruments for measurement of light absorption by aerosols. *Rev Sci Instrum*. 2000;71:4545.
- [4] Arnott WP, Walker JW, Moosmüller H, Elleman RA, Jonsson HH, Buzorius G, et al. Photoacoustic insight for aerosol light absorption aloft from meteorological aircraft and comparison with particle soot absorption photometer measurements: DOE Southern Great Plains climate research facility and the coastal stratocumulus imposed perturbation experiments. *Journal of Geophysical Research*. 2006;111.
- [5] Gyawali M, Arnott W, Lewis K, Moosmüller H. In situ aerosol optics in Reno, NV, USA during and after the summer 2008 California wildfires and the influence of absorbing and non-absorbing organic coatings on spectral light absorption. *Atmospheric Chemistry and Physics*. 2009;9:8007-15.
- [6] Lewis K, Arnott WP, Moosmüller H, Wold CE. Strong spectral variation of biomass smoke light absorption and single scattering albedo observed with a novel dual-wavelength photoacoustic instrument. *Journal of Geophysical Research*. 2008;113.
- [7] Moosmüller H, Chakrabarty R, Arnott W. Aerosol light absorption and its measurement: A review. *Journal of Quantitative Spectroscopy and Radiative Transfer*. 2009;110:844-78.
- [8] Slowik JG, Cross ES, Han JH, Davidovits P, Onasch TB, Jayne JT, et al. An inter-comparison of instruments measuring black carbon content of soot particles. *Aerosol Science and Technology*. 2007;41:295-314.
- [9] Abu-Rahmah A, Arnott WP, Moosmüller H. Integrating nephelometer with a low truncation angle and an extended calibration scheme. *Measurement Science and Technology*. 2006;17:1723-32.
- [10] Anderson TL, Ogren JA. Determining Aerosol Radiative Properties Using the TSI 3563 Integrating Nephelometer. *Aerosol Science and Technology*. 1998;29:57-69.
- [11] Chakrabarty RK, Arnold IJ, Francisco DM, Hatchett B, Hosseinpour F, Loria M, et al. Black and brown carbon fractal aggregates from combustion of two fuels widely used in Asian rituals. *J Quant Spectrosc Ra*. 2013;122:25-30.

- [12] Moosmuller H, Engelbrecht JP, Skiba M, Frey G, Chakrabarty RK, Arnott WP. Single scattering albedo of fine mineral dust aerosols controlled by iron concentration. *J Geophys Res-Atmos.* 2012;117.
- [13] Varma R, Moosmüller H, Arnott WP. Toward an ideal integrating nephelometer. *Opt Lett.* 2003;28:1007.
- [14] M MAP. Deriving the basic cell-reciprocal integrating nephelometer equation and its use for calibration purposes: a comprehensive approach. *Measurement Science and Technology.* 1999;10:R1-R15.
- [15] Sumlin BJ, Pandey A, Walker MJ, Pattison RS, Williams BJ, Chakrabarty RK. Atmospheric Photooxidation Diminishes Light Absorption by Primary Brown Carbon Aerosol from Biomass Burning. *Environ Sci Tech Let.* 2017.